Research Article | Vol. 24, No. 25 | 12 Dec 2016 | OPTICS EXPRESS 29048

Optics EXPRESS

X-ray absorption tomography employing a conical shell beam

J. P. O. Evans,[1,*] S. X. Godber,[2] F. Elarnaut,[1] D. Downes,[1] A. J. Dicken,[1] and K. D. Rogers[3]

[1]*Imaging Science Group, Rosalind Franklin Building, Clifton, Nottingham Trent University, Nottingham, UK*
[2]*Halo X-ray Technologies, MediCity, Nottingham, UK*
[3]*Cranfield Forensic Institute, Cranfield University, Shrivenham, Swindon, UK*
**paul.evans@ntu.ac.uk*

Abstract: We demonstrate depth-resolved absorption imaging by scanning an object through a conical shell of X-rays. We measure ring shaped projections and apply tomosynthesis to extract optical sections at different axial focal plane positions. Three-dimensional objects have been imaged to validate our theoretical treatment. The novel principle of our method is scalable with respect to both scan size and X-ray energy. A driver for this work is to complement previously reported methods concerning the measurement of diffracted X-rays for structural analysis. The prospect of employing conical shell beams to combine both absorption and diffraction modalities would provide enhanced analytical utility and has many potential applications in security screening, process control and diagnostic imaging.

OCIS codes: (110.7440) X-ray imaging; (110.6955) Tomographic imaging.

References and links

1. D. Bernardi, P. Macaskill, M. Pellegrini, M. Valentini, C. Fantò, L. Ostillio, P. Tuttobene, A. Luparia, and N. Houssami, "Breast cancer screening with tomosynthesis (3D mammography) with acquired or synthetic 2D mammography compared with 2D mammography alone (STORM-2): a population-based prospective study," Lancet Oncol. **17**(8), 1105–1113 (2016).
2. T. Gomi, M. Nakajima, H. Fujiwara, T. Takeda, K. Saito, T. Umeda, and K. Sakaguchi, "Comparison between chest digital tomosynthesis and CT as a screening method to detect artificial pulmonary nodules: a phantom study," Br. J. Radiol. **85**(1017), e622–e629 (2012).
3. A. P. Cuadros, C. Peitsch, H. Arguello, and G. R. Arce, "Coded aperture optimization for compressive X-ray tomosynthesis," Opt. Express **23**(25), 32788–32802 (2015).
4. I. Reiser and S. Glick, *Tomosynthesis Imaging* (Taylor and Francis CRC, 2014).
5. F. Xu, L. Helfen, T. Baumbach, and H. Suhonen, "Comparison of image quality in computed laminography and tomography," Opt. Express **20**(2), 794–806 (2012).
6. K. M. Dąbrowski, D. T. Dul, A. Wróbel, and P. Korecki, "X-ray microlaminography with polycapillary optics," Appl. Phys. Lett. **102**(22), 224104 (2013).
7. K. M. Dąbrowski, D. T. Dul, and P. Korecki, "X-ray imaging inside the focal spot of polycapillary optics using the coded aperture concept," Opt. Express **21**(3), 2920–2927 (2013).
8. M. T. Cole, R. J. Parmee, and W. I. Milne, "Nanomaterial-based X-ray sources," Nanotechnology **27**(8), 1–9 (2016).
9. M. Hassan, J. A. Greenberg, I. Odinaka, and D. J. Brady, "Snapshot fan beam coded aperture coherent scatter tomography," Opt. Express **24**(16), 18277–18289 (2016).
10. S. Singh and M. Singh, "Explosives detection systems (EDS) for aviation security," Signal Process. **83**(1), 31–55 (2003).
11. K. Wells and D. A. Bradley, "A review of X-ray explosives detection techniques for checked baggage," Appl. Radiat. Isot. **70**(8), 1729–1746 (2012).
12. G. Harding, "X-ray diffraction imaging--a multi-generational perspective," Appl. Radiat. Isot. **67**(2), 287–295 (2009).
13. A. Dicken, K. Rogers, P. Evans, J. W. Chan, J. Rogers, and S. Godber, "Combined X-ray diffraction and kinetic depth effect imaging," Opt. Express **19**(7), 6406–6413 (2011).
14. P. Evans, K. Rogers, J. Chan, J. Rogers, and A. Dicken, "High intensity X-ray diffraction in transmission mode employing an analog of Poisson's spot," Appl. Phys. Lett. **97**(20), 204101 (2010).
15. K. Rogers, P. Evans, J. Rogers, J. Chan, and A. Dicken, "Focal construct geometry – a novel approach to the acquisition of diffraction data," J. Appl. Cryst. **43**(2), 264–268 (2010).

#279656 http://dx.doi.org/10.1364/OE.24.029054
Journal © 2016 Received 2 Nov 2016; revised 30 Nov 2016; accepted 30 Nov 2016; published 7 Dec 2016

Optics EXPRESS

16. A. Dicken, A. Shevchuk, K. Rogers, S. Godber, and P. Evans, "High energy transmission annular beam X-ray diffraction," Opt. Express **23**(5), 6304–6312 (2015).
17. P. Kirkpatrick, "Theory and use of Ross filters II," Rev. Sci. Instrum. **15**(9), 223–229 (1944).
18. A. J. Dicken, J. P. O. Evans, K. D. Rogers, C. Greenwood, S. X. Godber, D. Prokopiou, N. Stone, J. G. Clement, I. Lyburn, R. M. Martin, and P. Zioupos, "Energy-dispersive X-ray diffraction using an annular beam," Opt. Express **23**(10), 13443–13454 (2015).
19. D. Prokopiou, K. Rogers, P. Evans, S. Godber, and A. Dicken, "Discrimination of liquids by a focal construct X-ray diffraction geometry," Appl. Radiat. Isot. **77**, 160–165 (2013).
20. F. Li, Z. Liu, and T. Sun, "Annular beam high-intensity X-ray diffraction based on an ellipsoidal single-bounce monocapillary," J. Appl. Cryst. **49**(2), 627–631 (2016).
21. P. Evans, K. Rogers, A. Dicken, S. Godber, and D. Prokopiou, "X-ray diffraction tomography employing an annular beam," Opt. Express **22**(10), 11930–11944 (2014).
22. Y. Levakhina, *Three-Dimensional Digital Tomosynthesis: Iterative Reconstruction, Artifact Reduction and Alterative Acquisition Geometry* (Springer, 2014).
23. J. Dörr, M. Rosenbaum, W. Sauer-Greff, and R. Urbansky, "Automatic focus algorithms for TDI X-Ray image reconstruction," Adv. Radio Sci. **10**, 145–151 (2012).
24. A. M. Beale, S. D. M. Jacques, E. K. Gibson, and M. Di Michiel, "Progress towards five dimensional diffraction imaging of functional materials under process conditions," Coord. Chem. Rev. **277–278**, 208–223 (2014).
25. A. J. Dicken, J. P. O. Evans, K. D. Rogers, N. Stone, C. Greenwood, S. X. Godber, J. G. Clement, I. D. Lyburn, R. M. Martin, and P. Zioupos, "Classification of fracture and non-fracture groups by analysis of coherent X-ray scatter," Sci. Rep. **6**, 29011 (2016).

1. Introduction

Three-dimensional imaging of opaque objects using X-rays is exploited extensively in medicine, industrial inspection and security screening. In recent years, tomosynthesis has undergone a resurgence of interest in diagnostic imaging applications such as breast cancer screening [1] and the detection of pulmonary nodules [2]. More advanced approaches have investigated coded apertures and multiple X-ray sources for compressive tomosynthesis to reduce radiation exposure [3]. The tomographic approach enables the reconstruction and visualisation of volumetric information from a series of slice images. The tomographic principle involves summing projections from different relative locations to effect a blurring out of structures either side of a plane of interest. In general, computed axial tomography (CAT) employs in-plane one-dimensional projections, while classical tomography or tomosynthesis [4] employs two-dimensional projections over a limited angular range. In particular, the shape of flat objects can produce highly attenuated projections in directions at or near the object plane. Under such conditions, the two-dimensional point projections employed typically in tomosynthesis can provide a more complete sampling of flat objects in comparison to CAT, which in contrast requires a 360° rotation about the normal to the X-ray beam [5].

Microlaminography [6,7] has been demonstrated by employing polycapillary optics to focus radiation from laboratory X-ray sources or synchrotrons into micro-spots to form an inspection volume. For example, lamellae structures found in integrated circuits placed within the focal spot can be imaged in a similar way to classical tomography but without the requirement for sample or source rotation [6]. Recent advances in the design and construction of X-ray sources [8] promises rapid switching to replace mechanical scanning with switched source alternatives.

Many applications would benefit from material composition or structural information attributed directly to spatially distributed components within an inspection volume. Recent advances in coded aperture coherent scatter tomography [9] have demonstrated the use of a fan beam of interrogating X-rays to ultimately, exploit object motion to produce a three-dimensional materials discriminating imaging system. Although, significant challenges in terms of spatially complex objects and cluttered scenes, which are prevalent in real-world applications, require further investigation and development. An important and challenging example is encountered in the security screening of air passenger luggage, which routinely employs X-ray absorption imaging to help detect shape-based threats such as guns, knives and sharps. In contrast, threats including narcotics and a wide range of plastic, liquid and

Optics EXPRESS

homemade explosives (HMEs) present highly shape-variant threats that also require material specific information for enhanced false-alarm resolution [10–12]. Given that coherently scattered X-rays occur naturally during the radiographic process and that X-ray diffraction is the 'gold standard' for conducting materials structural discrimination it is a very attractive proposition to combine both methods to reduce potentially false-alarm rates. We have previously reported; see Section 2.1, the benefits of depth-resolved materials characterization employing X-ray diffraction tomography along with other conical shell or annular beam techniques. If depth resolved absorption and diffraction imaging [12,13] were combined successfully in a compact and cost-effective technology, then it could be deployed to increase the throughput of carry-on and checked luggage at international travel hubs. This technological development would be a major and disruptive advance for material specific security screening applications.

To complement earlier annular beam work we present a study of the absorption contrast signals propagating along the direction of the primary beam. We demonstrate our method by scanning a multi-layered object through an annular beam of X-rays. The beam projections have been collected from a corresponding ring shaped region of interest on the input window of an X-ray image intensifier optically coupled to a CCD camera. Pixels recorded at fixed circumferential positions along the ROI are composited to form a sequence of oblique views during a two axis translational scan. This image sequence encodes the position of inspected object features along the normal to the scan direction as depth dependent circular parallax. The application of tomosynthesis enables the extraction of optical sections at corresponding axial focal plane positions. This bright field capability is highly promising as it supports and informs the earlier dark-field work in the ongoing development of a new material specific high-energy X-ray imaging modality.

Our paper is organised as follows. Section 2 presents the methods including the theory background, our new imaging technique and describes the experiment conditions. Section 3 presents our experiment results and discussion. Section 4 summarizes our conclusions, discusses the implications of our findings and the future direction of the work.

2. Methods

2.1 Theory background

We have previously reported an alternate X-ray diffraction technique employing conical shell or annular interrogating X-ray beams, termed focal construct technology (FCT). This approach detects the presence of Bragg maxima from polycrystalline samples in the form of high intensity focal spots along the symmetry axis of the interrogating beam. This work encompassed angular dispersive methods realized by either translating the detector [14,15] or the sample [16] along the symmetry axis of the beam; the latter method employed pseudo-monochromatic high energy X-rays (W-Kα) obtained via balance filtering [17]. We have also demonstrated an energy dispersive approach [18] in which both the sample and detector remain stationary to enable the recovery of high-energy polychromatic focal spots from a centrally positioned point detector. These methods deal favorably with non-ideal samples such as those exhibiting large grain size, preferred orientation and liquid samples [19], which exhibit only short-range order. Separate independent studies using low X-ray energies and mono-capillaries [20] have also demonstrated the validity of the FCT method. In addition, we have demonstrated depth resolved material specific imaging by analysing caustics [21] in the diffracted X-ray intensity. Our prior work with annular beams has dealt with the analysis of coherently scattered X-rays collected from within the central dark field encompassed by the beam. This paper describes a complementary bright field absorption FCT approach.

Optics EXPRESS

2.2 New imaging technique

Our imaging technique employs translational scanning of an object through a conical shell beam of X-rays, see Fig. 1. Successive overlapping annular projections are measured along the x and y axes during the scan.

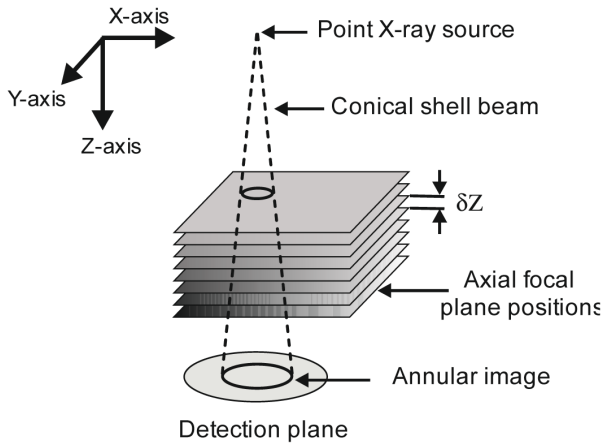

Fig. 1. A conical shell beam is incident normally upon a flat detector. The X-ray source and detector form a rigid body during the scan i.e. each undergoes a relative in-plane translation with respect to the object under inspection. The resultant focal plane positions within the inspection volume are parallel with the detection plane.

A value of intensity on the discretised annular absorption profile $i(\mathrm{r},\gamma)=i(v)$ is shown in Fig. 2.

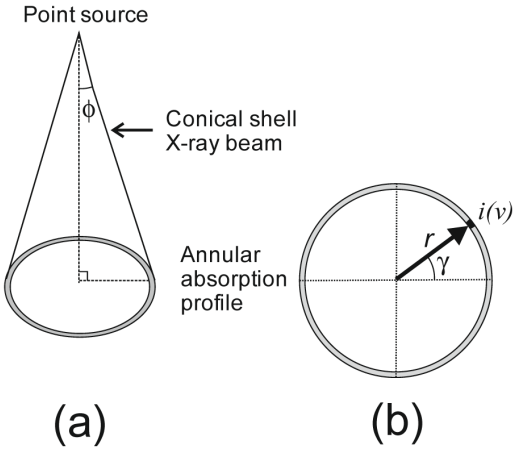

Fig. 2. (a) Conical shell interrogating beam with a half-opening angle of ϕ. (b) Discretised ring sample v with intensity i at polar coordinate (r,γ) where the pole is the piercing point of the symmetry axis on the detector plane.

Intensity values measured at a fixed polar coordinate position (r,γ) on each annular projection A may be composited to form an oblique projection C. Thus a succession of different oblique views D may be recovered from a matrix of coplanar annular projections B, as illustrated in Fig. 3.

Optics EXPRESS

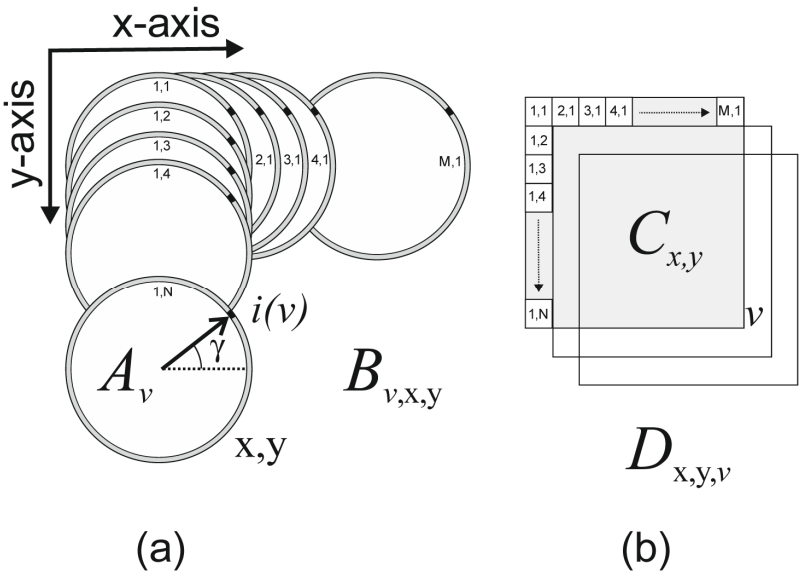

Fig. 3. (a) A sample position v at angle γ on an annular projection A; part of a series of coplanar annular projections B collected at discrete intervals along the x,y axes. (b) Composite oblique projection C comprised of pixels x, y associated with a fixed angular position γ (constant r value); part of a series of oblique projections D collected at discrete angular intervals in γ (or annular sample positions v).

A complete description of the pixel registration is given by

$$B_{v,\mathrm{x,y}} = A_{v_{(x,y)}} \qquad \forall x \in \{1...N\}, y \in \{1...M\} \tag{1}$$

$$D_{\mathrm{x,y},v} = C_{(x,y)_v} \qquad \forall v \in \{1...2\pi/\Delta\gamma\} \tag{2}$$

$$D_{x,y,v} = B_{v,x,y} \tag{3}$$

Where $\Delta\gamma$ is the increment in angular separation between neighbouring elements v composing the annular sensor. The total number of samples or pixels composing each oblique image equates to the product NM, which is determined by the total number of discrete annular projections. Although the total number of oblique images is determined by $V = 2\pi/\Delta\gamma$, this in practice is limited by the native resolution of the annular sensor. The conversion from a pixel separation along the x-axis or along the y-axis into linear distances is given by $m\delta x$ and $n\delta y$, respectively. Where n and m are the total number of pixels under consideration and, $\delta x, \delta y$ and are the step distances, respectively. The production of depth dependent circular parallax is recorded by the oblique projection series D. The diagram in Fig. 4 shows a focal plane position in object space together with the associated pseudo X-ray beam topology that equivalently applies when radially shifted oblique projections are considered.

Optics EXPRESS

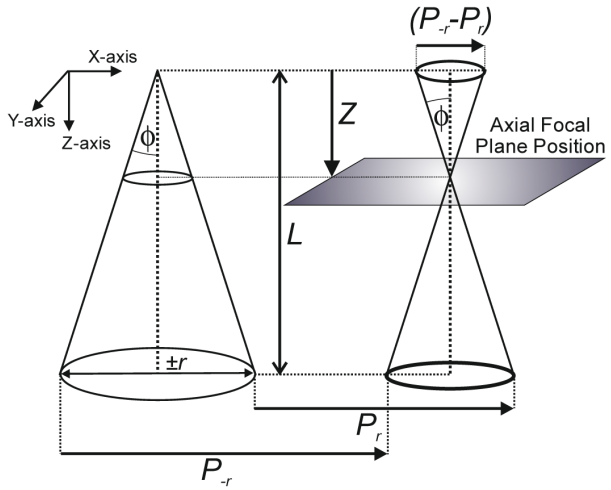

Fig. 4. A focal position is shown by considering coincident annular beam rays originating from a continuum of different point source locations during a rectilinear scan. The separation between conjugate points yields depth dependent parallax $\left(P_{-r}-P_{r}\right)$ where P_{-r} and P_{r} are linear distances measured with respect to reference locations at $\pm r$, respectively.

It can be appreciated from rotational symmetry that the magnitude of the parallax $\left(P_{-r}-P_{r}\right)$ is constant along polar directions $0\le\gamma\le 2\pi$ for a point in a given focal plane. The position is a function of the tomosynthesis half angle $\phi=\tan^{-1}\left(r/L\right)$ and is given by

$$Z=\frac{\left(P_{-r}-P_{r}\right)}{2\tan\phi}. \tag{4}$$

Where digital parallax $\left(p_{-r}-p_{r}\right)$ measured in the oblique image series D is related to parallax in object space by the following relationship $\left(P_{-r}-P_{r}\right)=\delta x\left(p_{-r}-p_{r}\right)$. To apply Eq. (4) requires employing shift-and-add tomosynthesis to recover the corresponding optical section. However, before presenting the digital tomosynthesis equation, Eq. (6), it will be helpful to consider the linear shift distance $S=\left(P_{-r}-P_{r}\right)/2$ to affect a focal plane in object space as a function of system parameters given by

$$S=Z\tan\phi. \tag{5}$$

It can be appreciated from this relationship, in combination with Fig. 4, that the inspection volume is bounded by two hypothetical focal planes; one is coincident with the point source plane $\left(Z=0,S=0\right)$ while the other is coincident with the detection plane $\left(Z=L,S=r\right)$. These conditions also bound the digitally reconstructed parameters.

A digital optical section T requires that the oblique projections D be shifted along their respective radial directions via two orthogonal axial components before being summed and averaged according to

$$T_{x,y}=\frac{1}{V}\sum_{v=0}^{V-1}D_{j,k,v} \tag{6}$$

where the digital shift indices j and k are given by

Optics EXPRESS

$$j = f\left[x, \frac{Z\tan\phi\cos(v\Delta\gamma)}{\delta x}\right] \tag{7}$$

$$k = f\left[y, \frac{Z\tan\phi\sin(v\Delta\gamma)}{\delta y}\right]. \tag{8}$$

In a practical system the value of parameters; $r, L, \phi, \delta x, \delta y, \Delta\gamma$ are all known and fixed for a given scan. It can be appreciated from Eqs. (7) and (8) that a one-to-one registration or common index (m,n) for all pixel positions composing the oblique projections occurs at $Z = 0$.

The separation between two neighboring focal plane positions, see Fig. 1, is obtained by differentiating Eq. (4):

$$\delta Z = \frac{\delta p}{2\tan\phi} \tag{9}$$

where $\delta p = \delta x$ is the minimum detectable increment in parallax.

2.3 Experiment setup

We employed an industrial X-ray inspection system (X-tek Systems VTX 160) to provide computerised control of X-ray source/imaging parameters and scanning of the phantom in a radiological inspection chamber. A micro-focus generator with a $2\,\mu m$ spot size and a tungsten transmission target produced the X-rays. The accelerating voltage and current were $70\,kV$ and $50\,\mu A$, respectively. Annular projections with a half-opening angle $\phi = 6.87^{\circ}$ were collected from a ring shaped ROI, $R = 53.37\,mm$, on a (Thales TH 9464 QX) 6" image intensifier with a CsI phosphor input screen. The separation between the input window of the intensifier and the point X-ray source was fixed, $L = 443\,mm$, throughout the experiments. The intensifier was optically coupled to an AVT Manta GigE camera capturing 1280 x 1024 x 8 bit images. The corresponding annular ROI from each frame was exposed for $70\,ms$.

To demonstrate the technique a multi-level phantom shown in Fig. 5 was fabricated to support a number of different thin $\approx 1\,mm$ steel shapes together with a "NTU logo" in copper laminate $\approx 0.3\,mm$ all arranged in arbitrary x,y positions upon radiotranslucent sheets.

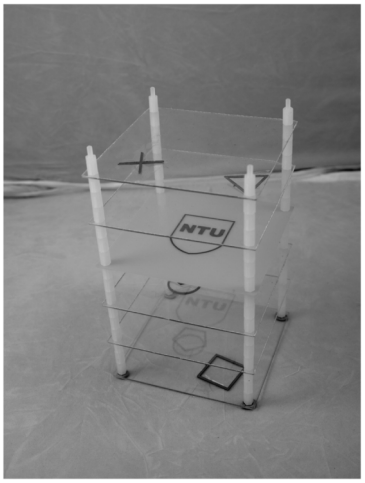

Fig. 5. Calibrated phantom comprising of thin metal shapes on plastic substrates.

Optics EXPRESS

The X-ray absorption contrast produced by the steel material against the relatively low density plastic material provided the image forming signal for our experiments. Also, the coordinate positions of the targets were carefully measured and recorded prior to scanning and image reconstruction; see true coordinate values presented in Table 1. The phantom was raster scanned through 400 positions along the x and y axes in steps of $\delta x = \delta y = 350\ \mu$m. This setup provided sufficient sampling to resolve the minimum feature size of ≈ 1 mm on the steel shapes in the oblique projections and in the resultant optical sections.

3. Results and discussion

3.1 Composite oblique projections

The phantom was placed within the inspection volume and was raster scanned along the x-axis and the y-axis according to the experiment conditions described in Section 2.3. The discrete annular projections A have been collected and stored as a series B; the resultant composite oblique projections C have been reconstructed on discrete (r, γ) positions and stored as a sequence D in digital memory according to Eqs. (1)-(3). An example of the composite images is shown in Fig. 6.

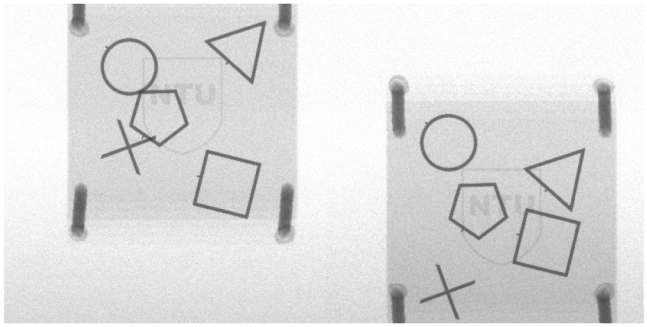

Fig. 6. Example of composite oblique images separated by an interval of π in γ (left $\pi/2$) and (right $3\pi/2$) from a sequence D comprised of 360 different views of the phantom.

The sequence D was comprised of $V = 360$ frames and demonstrates that spatially corresponding object features undergo a depth dependent circular translation. It can be appreciated that under the condition of a zero digital shift that the expression $(p_{-r} - p_r)$ describes the diameter of the resultant translation or circular parallax of coplanar (x, y) image features. Therefore, by considering an incrementally increasing shift value from $S = 0$ to $S = r$ a zero parallax plane can be observed to translate through the sequence from $Z = 0$ to $Z = L$, respectively. These "stationary" planes are an analogue of the optical sections produced by the tomosynthesis analyzed in the following, Section 3.2.

3.2 Optical sections

A series of optical sections T, see Fig. 7, have been produced by applying shift-and-add tomosynthesis according to Eqs. (6)-(8).

Optics EXPRESS

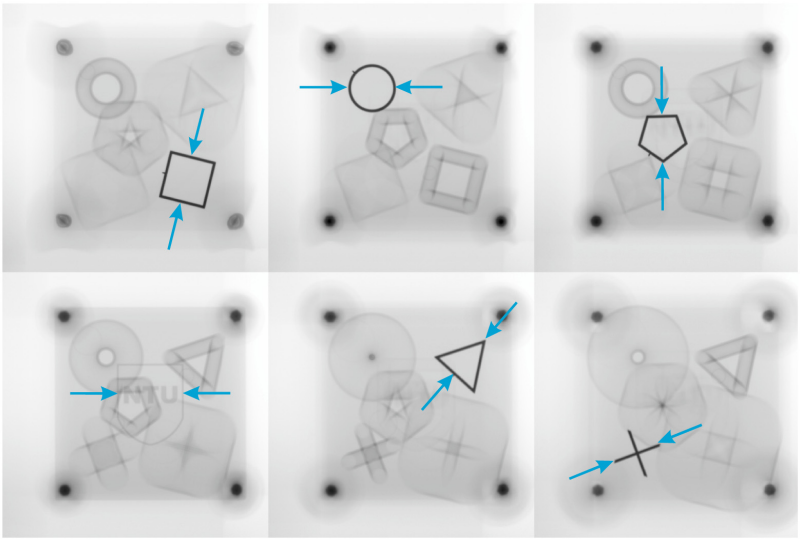

Fig. 7. Raw optical sections of the phantom at successive focal plane positions (Visualization 1). Out of plane object features appear increasingly blurred as a function of their axial separation from the focal plane position.

Table 1. Linear distances highlighted by the arrows in Fig. 7 are tabulated together with their corresponding true, and calculated values via Eq. (4).

	Distance (mm)	Square	Circle	Pentagon	NTU	Triangle	Cross
z-axis	True	106.0	138.0	169.0	201.0	230.0	262.0
	Calculated	107.5	138.0	168.5	200.5	230.0	261.5
(x,y) plane	True	25.0	25.0	25.0	35.0	25.0	26.5
	Calculated	25.2	25.2	25.2	35.0	25.2	26.6

The linear distances stated in Fig. 7, were computed from $m\delta x$ and $n\delta y$, where m and n are the corresponding distances in pixels. Again, the nominal 1:1 scale of the optical sections T was expected due to the equal scan step size, $\delta x = \delta y = 350\,\mu$m and independent of the annular beam half-opening angle $\phi = 6.87^{\circ}$ and the focal plane position as predicted by the theoretical analysis. The true z-axis positions of the optical sections recorded in Fig. 7 are plotted against parallax, measured in pixels, in the graph of Fig. 8.

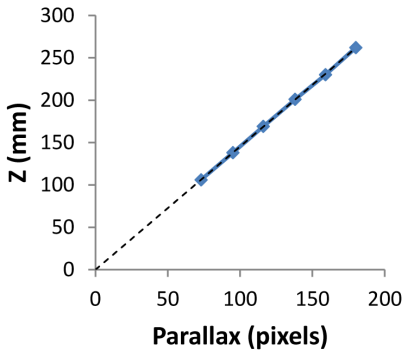

Fig. 8. True z-axis positions of six different optical sections plotted against parallax measured in pixels. Linear extrapolation shows a nominal intercept at the origin as z-axis distances were measured with respect to the point X-ray source.

Optics EXPRESS

The linear characteristic shown in the graph of Fig. 8 is expected when employing parallel projections to reconstruct optical sections. This aspect is a unique feature of our "point source" technique, which is also highlighted by the constant (object space to image space) magnification observed between the different optical sections recorded, see Fig. 7.

These observations are counter to those expected from conventional or circular tomosynthesis i.e. where the magnification factor associated with each optical section decreases as the distance to the axial focal plane increases. A change in magnification has a concomitant effect upon the discretized sample size along the x-axis and y-axis. In addition, the separation between adjacent axial focal plane positions $\delta z \propto z^2$. We did not observe any of these effects in the reconstructed x, y, z parameters recorded via annular beam tomosynthesis as supported and informed by the following analysis.

The linear regression line plotted in the graph of Fig. 8 has a gradient of $1.452\ mm/pixel$, as predicted by Eq. (9). This result is consistent with the expression for differential parallax $(p_{-r} - p_r)_a - (p_{-r} - p_r)_b$, from consideration of Eq. (4), being constant and independent of the shift value applied for two arbitrary points a and b located within the inspection volume. For example, the total number of predicted focal plane positions sandwiched between the square shape (nearest the source) and the cross shape (nearest the detector) of the phantom may be calculated from the difference between their respective shift values $\Delta S = 2(S_{top} - S_{bottom})$ as $\Delta S/\delta P = 2\tan\phi(262\ mm - 106\ mm)/350\ \mu m = 107.39$ pixels, from consideration of Eq. (5). This digital shift value may be expressed as a distance with the aid of Eq. (9) as $\Delta Z = \Delta S \delta z = 107.39 \times 1.45\ mm = 156\ mm$. Alternatively, the separation between optical sections along the z-axis was calculated from Eq. (4) employing measured digital parallax as $\Delta Z = 261.5\ mm - 107.5\ mm = 154\ mm$. The resultant error -1.3% represents <1.5 pixels error in the measurement of differential digital parallax across the full z-axis component of the phantom. This result is within the bounds of expected experimental error for digital measurements. Any other source of error such as the imperfect alignment of the source, detector and translation plane was assumed too small to be observed directly in our experiment results. Therefore, our theory accurately describes the reconstructed x, y and z parameters.

The previously presented calibrated phantom, shown in Fig. 5, was designed to emphasise the details of the approach and support the analysis of the reconstructed image parameters. To complement this work we present the reconstruction results of a "real-life" sample featuring an irregular and complex morphology. The cylindrical phantom, see Fig. 9, comprises of an aggregate of objects to represent a section through a luggage item to emulate a security screening application.

Optics EXPRESS

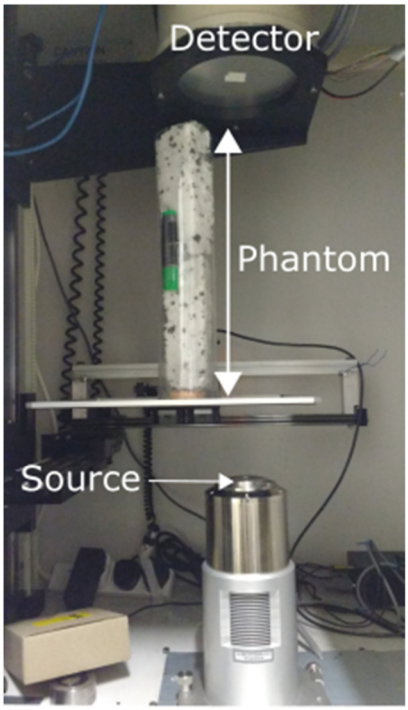

Fig. 9. Cylindrical phantom mounted on the translation table in the X-ray inspection system. An aggregate of discrete objects arranged along a ~38 cm component of the z-axis were supported by polystyrene foam.

Again, a series of optical sections T, see Fig. 10, have been produced by applying shift-and-add tomosynthesis according to Eqs. (6)-(8).

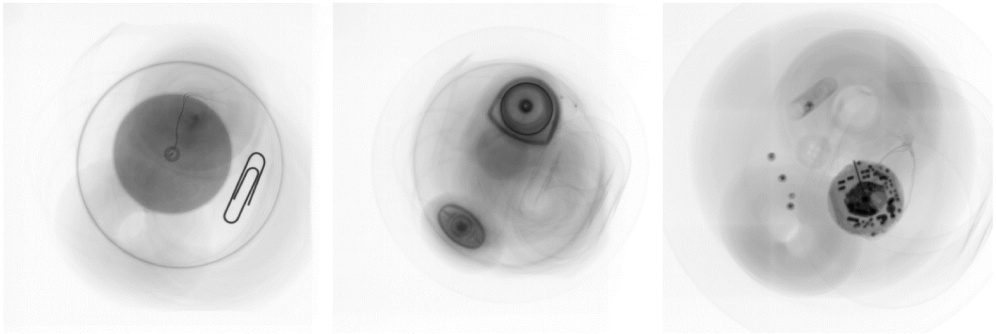

Fig. 10. Three optical sections of the cylindrical phantom: (left, nearest the source) a plastic Petri dish containing a disc of soap and a paperclip; (middle, around midway between the source/detector) elliptical cross-section of a plastic marker pen and the circular cross-section of the pressurised canister within a medical inhaler; (right, nearest the detector) printed circuit board (PCB) from a wristwatch. In addition, two fine gauge metal wires run the full length of the phantom. The wires can be observed as a twisted pair leading from a circular metal contact (source side) at the centre of the soap, and as two dots near the circular cross section of the pressurised canister, and finally in the rightmost image connecting to the PCB. The full series of raw optical sections at successive focal plane positions can be seen in (Visualization 2).

Optics EXPRESS

4. Conclusions and future work

We demonstrate that X-ray absorption signals can be optically encoded with the shape and location of object features along a conical shell beam. Optical sections of an object under inspection can be produced by employing an orthogonal two-axis raster scan. A key aspect of the approach is that the pixels, which compose an overlapping matrix of annular projections, can be composited to form oblique projections. The corresponding composite ray geometry is equivalent to an inclined parallel beam incident upon a rotating phantom or a rotating source of parallel X-rays about a stationary phantom. The angular separation between each "snapshot" is paramatised equivalently in our method by the angular separation between adjacent pixels in the ring images. This finding is counterintuitive as only linear motion was required during our image collection process i.e. there was no relative rotation of the object under inspection. The advantage of our method is that it enables the enhanced reconstruction fidelity provided by rotational tomosynthesis e.g. radial out of plane blurring as opposed to linear blurring [22] but still using linear translation i.e. a common industrial inspection requirement. Moreover, our proposed idea is scalable with respect to both scan size and X-ray energy and could be implemented for micro-imaging e.g. with polycapillary optics.

However, the initial driver for our novel technique is that supports the collection of caustics in the diffracted X-ray flux for structural analysis. We have previously demonstrated that diffracted X-rays can be encoded with the shape and location of the crystalline features along an annular beam [21]. In future experiments we plan to combine the collection of both absorption and diffraction data via a single conical shell beam to support and inform material phase analysis. This approach will require balancing carefully the requirements for X-ray absorption and X-ray diffraction signals. For example, as the X-ray beam energy is increased the scattering cross section and characteristic scatter angles both reduce. This scenario presents significant challenges in terms of sensing simultaneously both the relatively low intensity diffracted flux and the high intensity annular beam flux. Therefore, the work presented in this paper is a critical step towards realising combined absorption and diffraction FCT. In addition, our on-going work is pursuing multiple emitter X-ray sources for enhanced scanning speed. We believe that our approach has many potential applications where spatial distribution and structural information are both critically important e.g. security screening [10–12], process control [23, 24] and diagnostic bone 'quality' imaging [25].

Funding

U.S. Department of Homeland Security, Science and Technology Directorate through The Advanced X-Ray Material Discrimination Program (HSHQDC-15-C-B0036).